coatings

MDPI

Article

Effect of the TiN-to-CrN Layer Thickness Ratio on the Mechanical, Tribological and Corrosion Properties of TiN/CrN Multilayer Coatings

Kenzhegali Smailov [1,2], Aidar Kenzhegulov [1,*], Axaule Mamaeva [1], Nauryzbek Bakhytuly [1], Piotr Kowalewski [3], Arailym Mukangaliyeva [1] and Diana Karim [1]

[1] Institute of Metallurgy and Ore Beneficiation, Satbayev University, Almaty 050013, Kazakhstan; k.smailov@satbayev.university (K.S.)
[2] Faculty of Chemistry and Chemical Technology, Al-Farabi Kazakh National University, Almaty 050040, Kazakhstan
[3] Faculty of Mechanical Engineering, Department of Fundamentals of Machine Design and Mechatronic Systems, Wroclaw University of Science and Technology, Wroclaw 50-370, Poland
* Correspondence: a.kenzhegulov@satbayev.university; Tel.: +7-707-2000062

Abstract

TiN/CrN multilayer coatings with bilayer periods of 20 and 30 nm and TiN:CrN layer thickness ratios of 1:1, 1:2 and 2:1 were deposited on 40Kh steel substrates by pulsed direct current magnetron sputtering (pDCMS). The phase composition (XRD), microstructure (SEM), mechanical (nanoindentation, scratch testing), tribological (dry sliding and boundary lubrication), and corrosion (potentiodynamic polarization in 3.5 wt.% NaCl) characteristics of the coatings were examined. Increasing the TiN volume fraction increased nanohardness and elastic modulus reaching a maximum H^3/E^2 = 0.186 GPa. The Λ30-TiN(20)/CrN(10) coating showed the best adhesion (L_{c1} = 14.4 N, L_{c2} = 17.7 N, CPR_S = 48 N^2) and the lowest wear rate both under dry sliding and under boundary lubrication (1.2×10^{-5} $mm^3/(N\cdot m)$). In contrast, CrN dominance (Λ30-TiN(10)/CrN(20)) sharply degraded the tribological behaviour (the wear rate increased by almost an order of magnitude) and caused catastrophic localized pitting in the corrosion tests. At the same time, the best corrosion resistance ($E_{corr} \approx -0.47$ V, the most extended quasi-passive region) was achieved at the smallest bilayer period. A balanced composition, Λ20-TiN(10)/CrN(10), owing to the highest density of interlayer boundaries, effectively blocks through-thickness growth defects. The architectures that are optimal in terms of mechanical/tribological and of corrosion criteria do not coincide, which indicates that the TiN:CrN ratio has to be chosen according to the dominant type of service loading. The results obtained show that varying the thickness ratio of the TiN and CrN layers at bilayer periods of 20 and 30 nm makes it possible to tune the balance of hardness, wear resistance, adhesion and corrosion resistance of multilayer coatings on structural steels.

Keywords: TiN/CrN multilayer coatings; pulsed direct current magnetron sputtering; bilayer period; nanoindentation; scratch test; corrosion

Academic Editor: Shibo Li

Received: 25 August 2026
Revised: 14 September 2026
Accepted: 18 September 2026
Published: 19 September 2026

1. Introduction

Today, the requirements imposed on machine parts and equipment operating under load, friction, and wear (engine and machine components, pump and compressor parts,

stamping, pressing, and cutting tools, and others) are becoming ever more stringent. In an aggressive environment, these parts undergo not only tribological wear under mechanical loading but also inevitable attack by corrosive media. Under this combined attack, the surface of the parts degrades faster, which leads to destruction of the surface material. Premature failure results in considerable economic losses [1–3]. According to the generalized estimate of Holmberg and Erdemir, about 23% of global energy consumption is directly or indirectly related to tribological interactions, and roughly one third of this amount is due to losses caused by wear and the subsequent restoration of components [4]. Various structural alloy steels, including 40Kh steel (equivalent to AISI 5140, DIN 41Cr4), are widely used in the manufacture of pumps and shafts [5,6], but their corrosion and wear resistance is limited. Surface modification or treatment approaches are therefore needed that can simultaneously improve the corrosion and wear resistance of structural steels [7,8]. One effective way of solving this problem is to apply protective and antifriction coatings to the surface [9,10].

Among the surface modification techniques, physical vapour deposition (PVD) holds a leading position because it allows the controlled synthesis of dense, uniform films at temperatures that do not exceed the tempering temperature of most alloy steels [5]. Within this approach, coatings based on transition metal nitrides form a separate class of protective and antifriction systems, among which TiN/CrN multilayer coatings stand out because they combine accessible technology, a well-established deposition process and good in-service performance [5,11–13]. The microstructure and properties of TiN/CrN multilayers are closely related to the deposition parameters and to the coating architecture. Recent years have seen intensive study of the mechanical, tribological, and corrosion properties of these coatings. The overwhelming majority of published work focuses on varying the bilayer period Λ at a fixed TiN/CrN layer thickness ratio of 1:1. For XC48 steel, for example, it has been shown that decreasing Λ from ≈240 to ≈12 nm at equal TiN and CrN fractions raises the nanohardness of the multilayer above 40 GPa and the Young modulus above 600 GPa through an increase in the number of interfaces up to ≈300 [14]. Paulitsch et al. [15] found that reducing Λ from 7.8 to 6.4 nm lowers the friction coefficient of CrN/TiN from 0.7 to 0.35. Decreasing Λ at equal layer fractions also improves the sliding resistance under dry friction conditions.

At the same time, systematic studies in which the period Λ is kept constant while the TiN/CrN thickness ratio itself is varied remain scarce. For example, Tu et al. [16], using a hybrid HiPIMS/AIP technology to deposit Cr_2N/TiN with a thickness ratio of ~158 nm Cr_2N to 28 nm TiN, obtained a maximum hardness of 25.1 GPa and an adhesion level of HF1. The hexagonal Cr_2N phase, which forms when the N_2 flow to the Cr target is insufficient, disrupts the coherence of the interfaces and suppresses the superlattice strengthening mechanism. Su et al. [17] showed that when the ratio is shifted in favour of TiN (TiN:CrN = 2:1), the optimum period shifts to Λ ≈ 15–20 nm because of the changed geometry of the interfacial stresses.

At a constant bilayer period, the ratio of the individual TiN and CrN layer thicknesses acts as an independent variable that governs the structure and the resulting properties of TiN/CrN multilayers. It is this ratio that determines the volume fractions of two phases with opposite functional roles: TiN carries the main load and provides the load-bearing capacity, whereas CrN is responsible for ductility, corrosion resistance, and the reduction in residual compressive stresses in the system. Changing the TiN:CrN thickness ratio at a fixed Λ makes it possible to re-tune the balance between strength and toughness without changing the number of interfaces or the overall density of crystalline boundaries. This decouples the effect of the phase fractions from that of the interface density in the formation of the service characteristics. Moreover, for medium-strength structural chromium steels such as 40Kh, studies of multilayer TiN/CrN systems are few, although it is precisely

for this group of materials that the problem of the protective properties of the coating is most acute [5,8].

Thus, an analysis of the current literature shows that most studies deal with TiN/CrN coatings with a constant Λ in the superlattice range (Λ < 30 nm), whereas the effect of the thickness ratio of the constituent layers at a fixed Λ = 20–30 nm remains systematically unexplored within a single experiment. Accordingly, in the present work, pDCMS was used to deposit TiN/CrN multilayer coatings with bilayer periods of 20 and 30 nm and a varying TiN/CrN thickness ratio on 40Kh steel substrates. The phase composition, microstructure, mechanical properties, and tribological and corrosion characteristics of the resulting systems were studied under dry sliding and under boundary lubrication. The work aims to reveal the controlling influence of the ratio of the functional layers within the studied range of modulation periods on the formation of the protective and antifriction characteristics of the TiN/CrN system, and to identify the composition that provides the optimum balance of hardness, adhesion, wear resistance, and corrosion resistance of the coatings.

2. Materials and Methods

2.1. Substrate Preparation and Coating Deposition

The TiN/CrN multilayer coatings were deposited on the surface of 40Kh steel (⌀58 mm × 2 mm), p-type single-crystal silicon Si(100) wafers (SW GmbH, Schramberg, Germany), and A99 aluminum foil (Eurofoil Luxembourg S.A., Dudelange, Luxembourg) by pDCMS. The steel substrates were used for the tribological tests, the silicon for imaging the morphology and cross-section of the coating, and the foil for preparing powder samples of the coating for X-ray phase analysis. Prior to deposition, the 40Kh steel substrates (GOST 4543-2016 [18]) (Severstal, Cherepovets, Russia) were ground on abrasive papers up to P2000 grit, mirror-polished with diamond paste to a final particle size of 1 μm, and ultrasonically degreased in absolute ethanol for 20 min. Table 1 lists the chemical composition of the steel. The nitride layers were grown from separate titanium (VT1-0, 99 mm in diameter) and chromium (ERKh-1, 75 mm in diameter) targets, the chemical compositions of which are specified by GOST 19807-91 [19], and TU 14-22-164-2002 [20] and summarized in Tables 2 and 3. A fixed target-to-substrate distance of 30 cm was maintained during all deposition runs.

The working chamber was evacuated to a base pressure of 5×10^{-3} Pa before each deposition run. All substrates were subsequently ion-cleaned for 10 min in argon at 0.3 Pa using an APEL-IS-21CELL ion source (Applied Electronics, Tomsk, Russian Federation) operated at a plasma current of 50 mA and an accelerating voltage of 2.0 kV. The TiN and CrN nanolayers were then grown from two separate magnetrons, an APEL-MRE100 for titanium and an MKE-95/100 for chromium (Applied Electronics, Tomsk, Russian Federation). The magnetron discharge was powered by an APEL-M-5PDC-1000A-1 pulsed DC power supply (Applied Electronics, Tomsk, Russian Federation) operating in current-regulation mode. Both magnetrons were driven from this unit through separate output channels at a pulse repetition frequency of 60 kHz and a duty cycle of 65%, which corresponds to a pulse period of 16.7 μs with a pulse-on time of 10.8 μs and a pulse-off time of 5.8 μs. The discharge current was set to 2.0 A for the titanium target and 0.7 A for the chromium target. The substrate bias was supplied by a separate power supply operating in continuous (non-pulsed) DC mode and was kept constant at −100 V throughout the deposition. The flow rates of the inert and reactive gases were regulated by RRG-12 mass flow controllers (Eltochpribor, Moscow, Russian Federation), with argon serving as the inert gas and nitrogen as the reactive gas, both of 99.999% purity. A titanium adhesion layer 200 nm thick was deposited first to improve the bonding between the coating and the steel substrate. The deposition parameters of all the coatings obtained are given in Table 4. All

other process parameters were kept unchanged except for the sputtering time, since each layer has its own deposition rate. Three variants of TiN/CrN multilayer coatings with different layer thickness ratios were deposited, as shown schematically in Figure 1: 1/1, 1/2 and 2/1. These samples are designated as ΛX-TiN(a)/CrN(b), where ΛX corresponds to the bilayer modulation period and the numbers in parentheses correspond to the thicknesses of the individual TiN and CrN layers expressed in nanometres. The three coatings form two comparison pairs. Λ30-TiN(10)/CrN(20) and Λ30-TiN(20)/CrN(10) have the same bilayer period of 30 nm and differ only in which layer is thicker, which isolates the effect of the TiN:CrN ratio at a constant number of interfaces. Λ20-TiN(10)/CrN(10) serves as the symmetric reference with equal layer thicknesses. Table 5 lists the main characteristics of the coatings obtained.

Table 1. Chemical composition of 40Kh steel according to GOST 4543-2016 [18].

Steel Grade	C, %	Si, %	Mn, %	Ni, %	S, %	P, %	Cr, %	Cu, %
40Kh	0.36–0.44	0.17–0.37	0.5–0.8	≤0.3	≤0.035	≤0.035	0.8–1.1	≤0.3

Table 2. Chemical composition of VT1-0 titanium according to GOST 19807-91 [19].

Titanium Grade	Ti, %	Fe, %	Si, %	C, %	O, %	N, %	H, %	Others
VT1-0	99.24–99.7	≤0.25	≤0.1	≤0.07	≤0.2	≤0.04	≤0.01	≤0.30

Table 3. Chemical composition of ERKh-1 chromium according to TU 14-22-164-2002 [20].

Chromium Grade	Cr, %, Min	O, μg/g (ppm), Max	N, μg/g (ppm), Max	C, μg/g (ppm), Max	S, μg/g (ppm), Max	Fe, μg/g (ppm), Max
ERKh-1	99.95	50	50	80	20	80

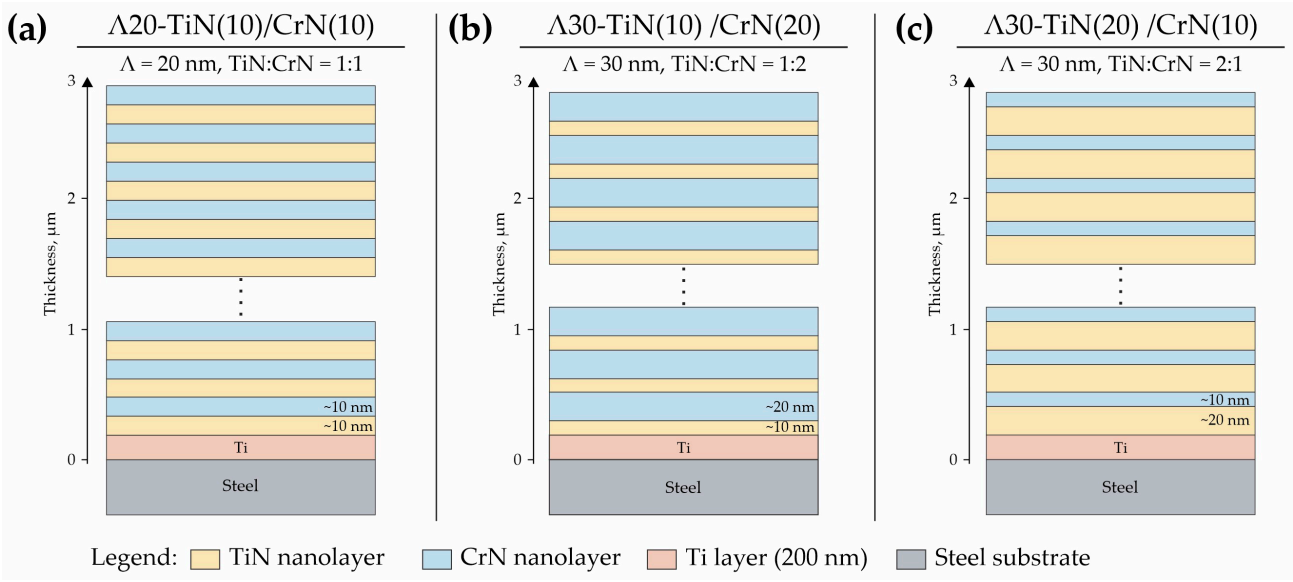

Figure 1. Schematic illustration of the architecture of the deposited TiN/CrN multilayer coatings with different TiN-to-CrN layer thickness ratios: (**a**) Λ20-TiN(10)/CrN(10); (**b**) Λ30-TiN(10)/CrN(20); (**c**) Λ30-TiN(20)/CrN(10).

Table 4. pDCMS parameters used for the deposition of the TiN/CrN multilayer coatings.

Coating Designation	Coating Deposition Parameters			
	Sputtering Time, min	Chamber Pressure, Pa	Inert and Reactive Gas Flow, L/h	Target Current, A
Λ20-TiN(10)/CrN(10)	112.5	0.4	For TiN: argon 1.1 + nitrogen 0.08 For CrN: argon 1.1 + nitrogen 0.35	Ti = 2; Cr = 0.7
Λ30-TiN(10)/CrN(20)	95	0.4		Ti = 2; Cr = 0.7
Λ30-TiN(20)/CrN(10)	130	0.4		Ti = 2; Cr = 0.7

Table 5. Main parameters and characteristics of the TiN/CrN multilayer coatings.

Coating Designation	Bilayer Period and Layer Ratio TiN/CrN	Thickness of the Multilayer Coating, μm and Number of Layers	Average Roughness (Ra), nm	Deposition Rate, nm/min
40Kh steel (substrate)	–	–	11	
Λ20-TiN(10)/CrN(10)	Λ = 20 nm, 10 nm/10 nm	2.8–260	23	25
Λ30-TiN(10)/CrN(20)	Λ = 30 nm, 10 nm/20 nm	2.8–173	35	29
Λ30-TiN(20)/CrN(10)	Λ = 30 nm, 20 nm/10 nm	2.75–173	14	21

2.2. Coating Characterization

The phase composition of the TiN/CrN multilayer coatings was examined by X-ray diffraction (XRD) on a D8 Advance diffractometer (BRUKER, Ettlingen, Germany) with Cu-Kα_1 radiation ($\lambda \approx 1.540598$ Å). Powder samples for the analysis were prepared by depositing the coatings onto aluminum foil and subsequently separating them from the substrate. The patterns were recorded over $2\theta = 4$–$90°$ with a step size of 0.01° and a scan rate of 0.1–1°/min at 35 kV and 20 mA. Phase identification was performed with the EVA-Search/Match module against the Powder Diffraction File PDF-2 rel. 2023 database. The same module computed the degree of crystallinity automatically as the ratio of the integrated intensity of the crystalline reflections to the total integrated intensity of the pattern after background subtraction; these values serve for comparison within the series and are not treated as absolute quantities.

The surface morphology and the cross-sections of the multilayers were examined by scanning electron microscopy (SEM) on a JXA-8230 microscope (JEOL, Tokyo, Japan), and the elemental composition was determined on the same instrument by wavelength-dispersive X-ray spectroscopy (WDS). Each measurement was averaged over several 100 μm × 100 μm areas of the coating surface. Samples deposited on silicon substrates were used both for imaging the morphology and for measuring the coating thickness.

The mechanical characteristics were determined by nanoindentation on a Fischerscope HM2000 S system (Helmut Fischer, Sindelfingen, Germany) equipped with a four-sided Vickers diamond pyramid with a face angle of 136°, in accordance with DIN EN ISO 14577 [21]. The nanohardness and the elastic modulus were measured at a load of 20 mN, an indenter approach speed of 2 μm/s, a load-setting accuracy of 0.4 mg, a displacement accuracy of 0.1 nm, and a creep time of 5 s at maximum load. Ten indents were made on

each coating, and the mean values are reported with the standard deviation. The indentation depth did not exceed 200 nm, which is below 10% of the coating thickness and therefore satisfies the conventional 10% rule for instrumented indentation, ensuring that the substrate does not affect the measured hardness.

The adhesion was evaluated by scratch testing on a Revetest RST 300 tester (Anton Paar, Graz, Austria) in the progressive loading mode with a Rockwell diamond indenter of 200 μm tip radius. The normal load was raised linearly from 0.5 to 30 N at 60 N/min over a scratch length of 4 mm at a travel speed of 4 mm/min. The normal load (Fn), the acoustic emission signal (AE), the friction coefficient (COF), and the penetration depth (PD) were recorded continuously throughout each test.

The tribological characteristics were evaluated on a TRB3 tribometer (CSM Instruments, Peseux, Switzerland) in the ball-on-disc configuration at room temperature and a relative humidity of 40–60%, following DIN 50324 [22]. Coated steel substrates were tested both under dry sliding and with a lubricant, with an Al_2O_3 ball 3 mm in diameter as the counterbody. The dry tests were run at a normal load of 2 N for 1000 cycles and the lubricated tests at 5 N for 2000 cycles, in both cases at a track radius of 5 mm and a sliding speed of 1 cm/s. The COF was recorded in real time, and the wear rate (WR) was calculated from the cross-sectional area of the wear track measured with a Surtronic S-128 profilometer (Taylor Hobson, Barcelona, Spain).

Three-dimensional topography and surface roughness of the coatings on the steel substrate were measured with a Leica DCM8 3D profilometer (Leica, Wetzlar, Germany) designed for surface metrology. The measurements were performed after the friction tests in order to obtain 3D micrographs of the wear and to characterize it. In this study, each wear track was scanned separately at three sites in the confocal mode using a 10× objective. The scanned areas were approximately 2 mm × 2 mm. The topographic data obtained were processed with the LeicaMap DCM software.

The electrochemical corrosion properties of the coated samples were studied with a potentiostat/galvanostat Corrtest 350M (CorrTest Instruments, Wuhan, China) in a 3.5 wt.% NaCl solution. A standard cell with a three-electrode system was used for the corrosion tests, in which a platinum plate served as the counter electrode, Ag/AgCl as the reference electrode, and the coated sample as the working electrode. The circular area of the coating surface under study on the steel was 0.785 cm^2. To reach a stable steady-state corrosion potential, the open circuit potential (OCP) was measured for 30 min before each test. The potentiodynamic polarization curves were recorded from −0.25 V to +0.25 V relative to the open circuit potential at a scan rate of 0.5 mV/s.

3. Results and Discussion

3.1. Structure and Composition of the TiN/CrN Multilayer Coatings

Figure 2 shows the XRD patterns of the TiN/CrN coatings deposited with different layer ratios. The patterns clearly show that all the coatings exhibit the main reflections from the (111), (200), and (220) planes of the cubic TiN and CrN phases. The coatings grow predominantly with a (200) orientation. The phases formed are mainly of a nitride structure based on TiN, CrN, and the possible (Cr,Ti)N solid solution. The pronounced overlap of the nitride peaks is due to the close lattice parameters of these phases, which is typical of nanoscale multilayer TiN/CrN systems, where partial mutual dissolution of Ti and Cr at the interlayer boundaries is possible [17,23,24]. As the CrN fraction increases, the full width at half maximum (FWHM) of the (111) and (200) peaks increases noticeably, which means that a higher CrN phase fraction reduces the crystallinity of the coating structure. The XRD analysis showed that the Λ30-TiN(10)/CrN(20) has a crystallinity of 28%, whereas the other coatings gave Λ20-TiN(10)/CrN(10) = 43% and Λ30-TiN(20)/CrN(10) = 50%. Overall, the data obtained confirm that varying the TiN and CrN layer thicknesses

allows the phase ratio to be changed in a controlled way without altering the nitride nature of the coating, which is an important advantage for optimizing the mechanical and tribological properties of TiN/CrN multilayers.

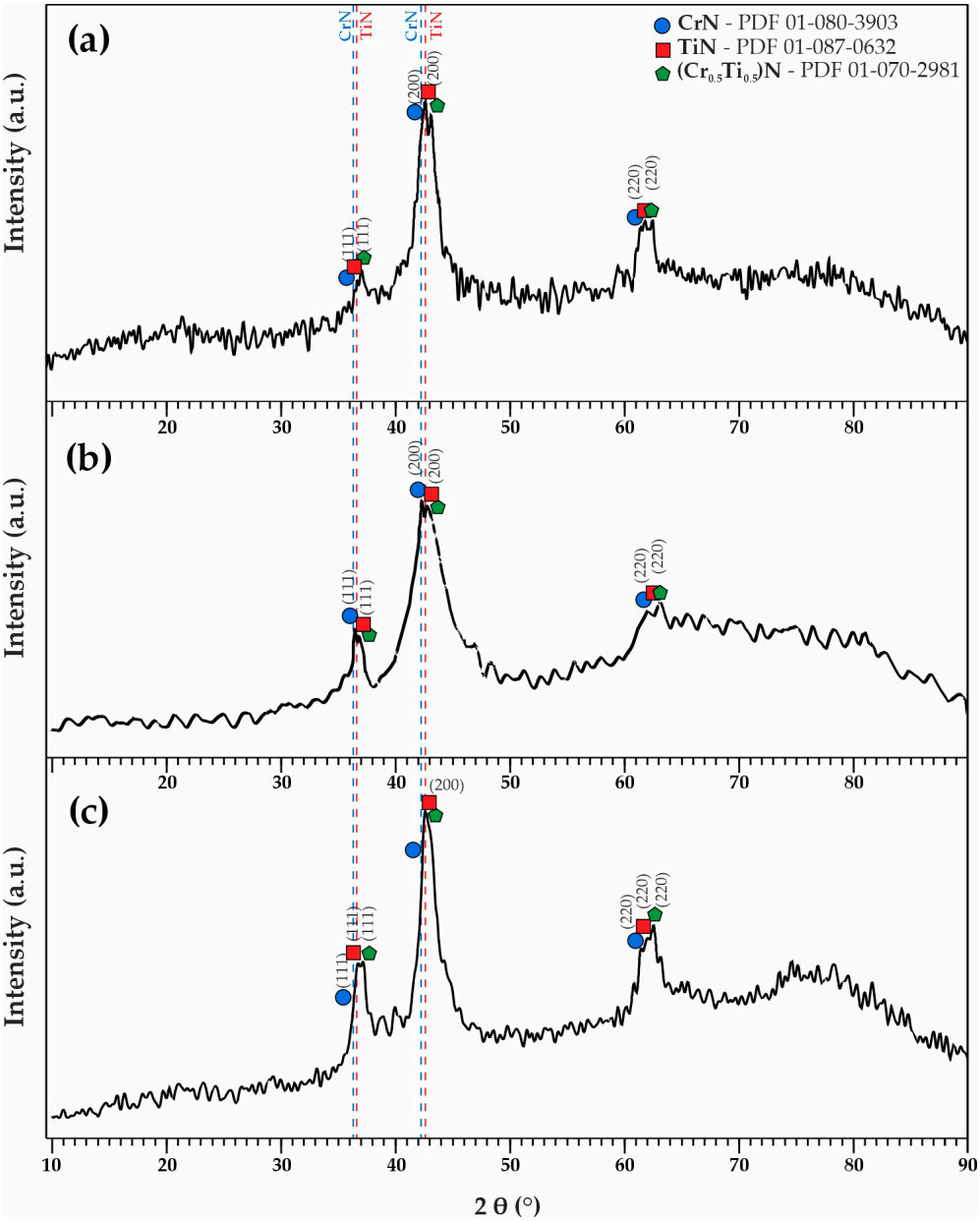

Figure 2. XRD patterns of the TiN/CrN multilayer coatings obtained: (**a**) Λ20-TiN(10)/CrN(10); (**b**) Λ30-TiN(10)/CrN(20); (**c**) Λ30-TiN(20)/CrN(10).

Micrographs of the surface morphology and cross-section of the TiN/CrN multilayers, which have different layer thickness ratios, are shown in Figure 3. As can be seen from the figure, continuous, even layers of fairly uniform thickness are formed. In all the variants studied the coating surface is smooth and even, with no pronounced cracks or fractured areas. The low density of pores and nucleation centres on the surface of the coatings studied is a natural consequence of the physics of magnetron sputtering combined with the multilayer architecture of the TiN/CrN system [14,25,26]. According to the cross-sectional data, the thicknesses of the Λ20-TiN(10)/CrN(10), Λ30-TiN(10)/CrN(20) and Λ30-TiN(20)/CrN(10) coatings are about 2.8, 2.8 and 2.75 μm, respectively. In all cases, the coating also retains a sharp boundary with the substrate with no signs of delamination.

The chemical composition analysis of the TiN/CrN multilayers revealed the main elements forming the nitride layers (Ti, Cr, and N) as well as oxygen. The contents of all the elements for each coating are given in Table 6. The results show that titanium and chromium vary in the range 19.1–31.9 at.% and 19.8–27 at.%, respectively. Nitrogen varied from 33.6 to 44.2 at.%. On the whole, this corresponds to the specified thickness ratios of the TiN and CrN layers in the coatings studied. Such differences may be related both to the changing fraction of the TiN and CrN nitride layers within the period and to the specific features of the quantitative determination of light elements by WDS. The oxygen content of 9.7–14.7 at.% is of extrinsic origin. The base pressure of 5×10^{-3} Pa leaves residual water vapour and oxygen, which are gettered by Ti and Cr during growth. Additional oxygen is taken up along the column boundaries of the coating during venting and air exposure, well beyond the native surface oxide [27,28]. Part of the reported value is also a normalization artefact, since nitrogen is underestimated by WDS in Ti-containing nitrides. No oxide reflections appear in the XRD patterns. The (Ti+Cr)/N ratio is 1.0–1.5. The value (Ti+Cr)/N ≈ 1 obtained for the Λ30-TiN(10)/CrN(20) coating indicates a composition close to the stoichiometric mononitrides TiN and CrN, for which a metal-to-nitrogen ratio close to 1:1 is typical [17,24,29]. The increase in this ratio to 1.3–1.5 for the other coatings may be caused by oxygen, which partially reduces the relative nitrogen fraction in the normalization of the WDS analysis.

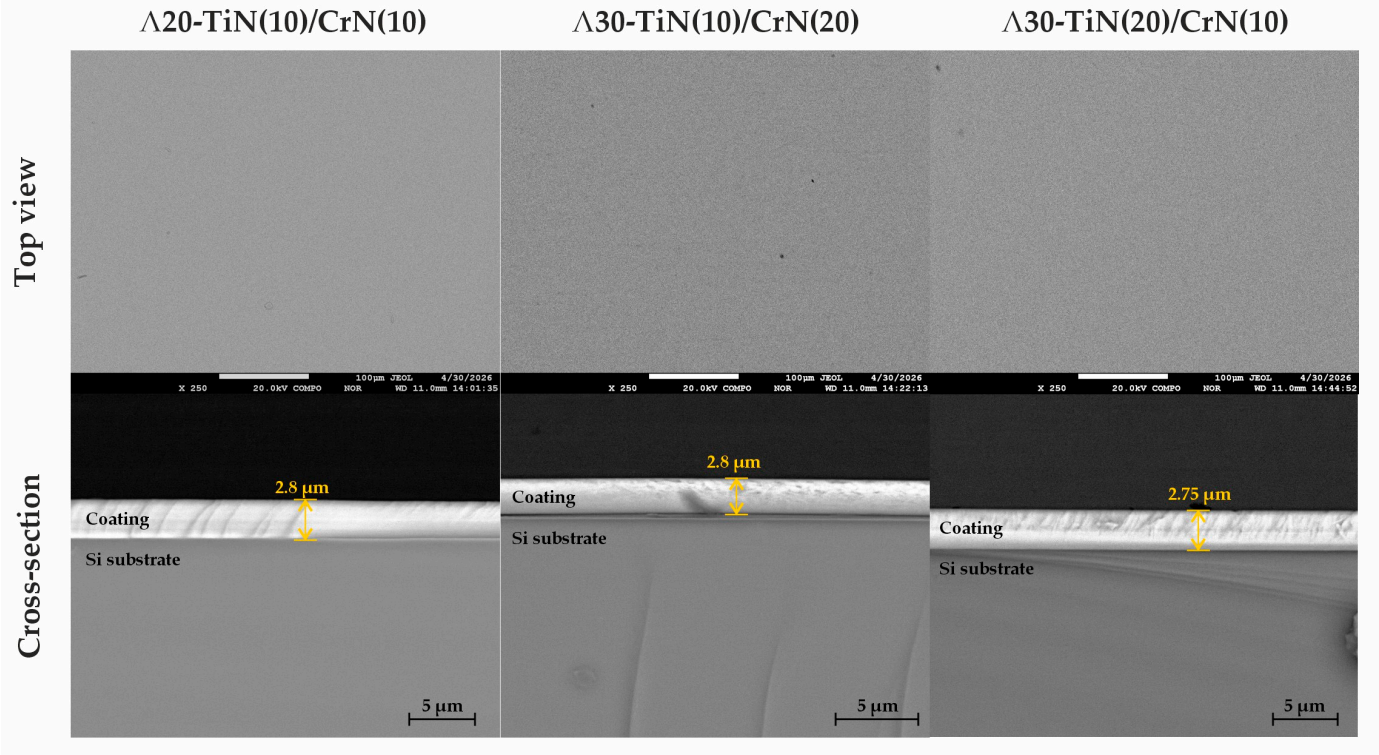

Figure 3. Surface morphology and cross-section view of the TiN/CrN multilayer coatings.

Table 6. Chemical composition of the TiN/CrN multilayers deposited with different layer ratios.

Coating Sample	Elemental Composition, at.%				(Ti+Cr)/N
	Ti	Cr	N	O	
Λ20-TiN(10)/CrN(10)	27.7	22.9	38.5	10.9	1.3
Λ30-TiN(10)/CrN(20)	19.1	27	44.2	9.7	1.0
Λ30-TiN(20)/CrN(10)	31.9	19.8	33.6	14.7	1.5

3.2. Analysis of the Mechanical Characteristics of the TiN/CrN Multilayer Coatings

Figure 4 shows the hardness (H) and elastic modulus (E) of the multilayers and of the steel substrate, where the coating hardness varies with the layer ratio. The elastic modulus follows a similar trend of gradual increase (Figure 4a). As the TiN fraction in the multilayer coating increases, the structure becomes denser and more crystalline, and the number of internal defects decreases, which leads to higher hardness. Raising the TiN volume fraction shifts the effective H and E values towards those of TiN itself, which, under identical deposition conditions, exceeds CrN by 15–20% in nanohardness and by 20–30% in elastic modulus owing to the higher energy of the Ti–N covalent-ionic bond [8,30–32]. The (200) texture does not follow the hardness trend: it is most pronounced in Λ20-TiN(10)/CrN(10). The hardness increase is therefore governed by the TiN volume fraction rather than by the growth orientation. In addition, another possible reason is the minimum average roughness R_a = 14 nm in this series, which ensures correct contact of the indenter without distortion of the signal by the surface relief [14]. Figure 4b shows the averaged indenter penetration depth-load curves for each coating; on average, the depth did not exceed 200 nm.

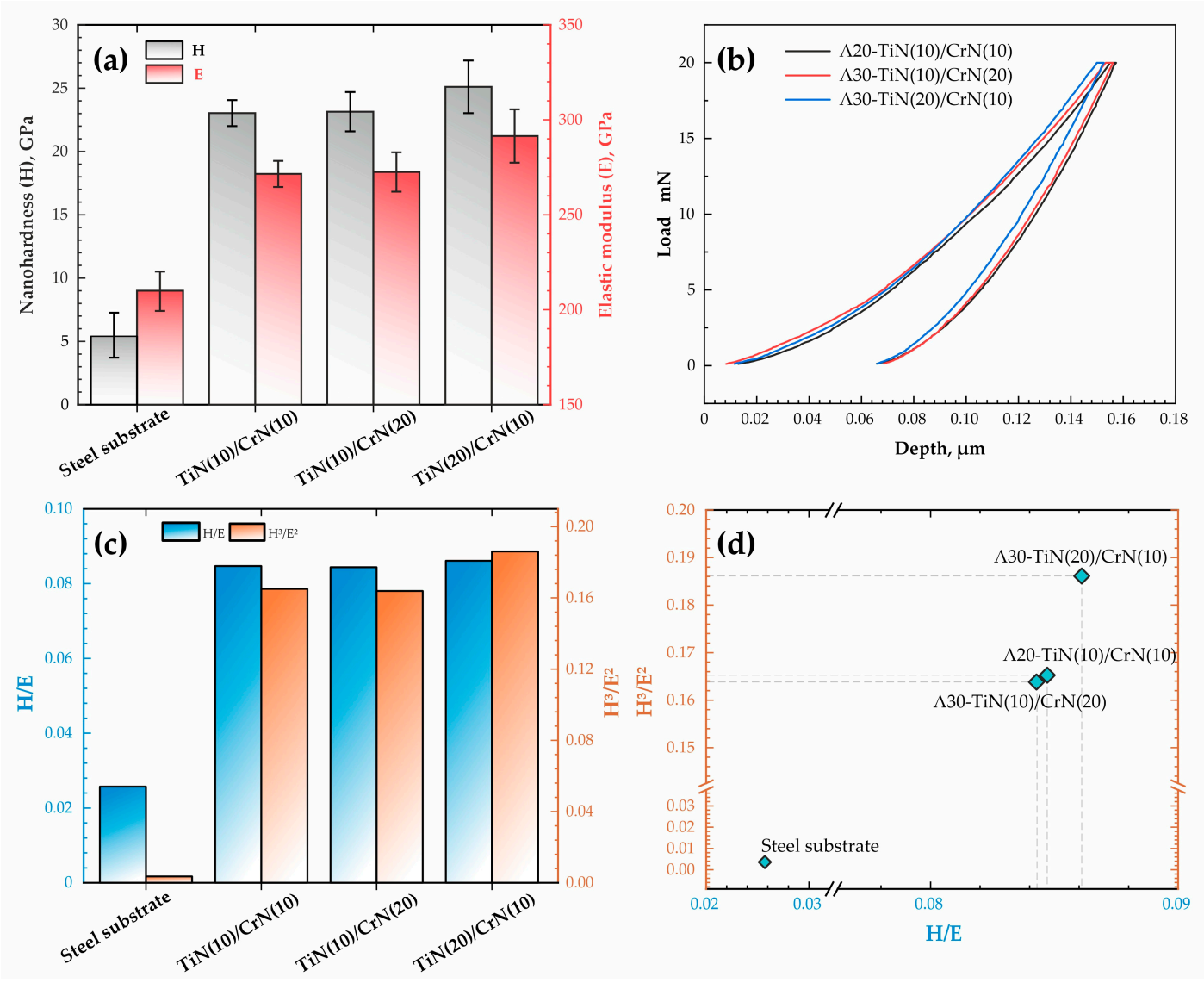

Figure 4. Mechanical characterization of the TiN/CrN multilayer coatings: (**a**) nanohardness and elastic modulus; (**b**) load–depth curves from nanoindentation tests; (**c**) H/E and H^3/E^2 ratios; (**d**) H^3/E^2 as a function of H/E.

The metal-to-nitrogen ratio may also contribute to the hardness variation. Vacancies in substoichiometric TiN_x and CrN_x can either increase hardness through vacancy hardening or reduce it through the loss of covalent Ti–N bonds. In the present series, however, hardness does not follow stoichiometry. The hardest coating, Λ30-TiN(20)/CrN(10), shows the lowest apparent nitrogen content and the highest (Ti+Cr)/N ratio. The apparent nitrogen content also decreases monotonically with increasing titanium content, which is consistent with the known underestimation of nitrogen by WDS in Ti-containing nitrides. The hardness increase is therefore attributed mainly to the higher intrinsic hardness of TiN. A secondary contribution of stoichiometry cannot be excluded.

Figures 4c,d show the H/E and H^3/E^2 ratios, which are key indicators of the fracture resistance of a coating. The H/E value reflects the ability of a coating to resist elastic deformation damage, whereas H^3/E^2 indicates its ability to resist plastic deformation [32,33]. Here again, the Λ30-TiN(20)/CrN(10) coating retains its advantage over the others because of its higher nanohardness and elastic modulus. The distribution map (Figure 4d) illustrates this clearly. According to the Leyland-Matthews criterion, all the coatings show H/E > 0.08, which corresponds to a high elastic strain to failure and excellent resistance to abrasive wear [34]. The value H^3/E^2 = 0.186 GPa for the Λ30-TiN(20)/CrN(10) coating is the highest in the series and 52 times higher than that of the substrate. According to the Musil criterion, this indicates a high resistance to plastic deformation in the contact zone [35].

The scratch test results of the coatings are shown in Figures 5a,b. In the scratch test, the critical loads L_{c1} (onset of coating cracking) and L_{c2} (onset of coating delamination) were determined. The adhesion and strength of a coating can be characterized by the crack propagation resistance index (CPR_s). The formula was calculated using Equation (1) [36]:

$$CPR_s = L_{c1} \cdot (L_{c2} - L_{c1}) \quad (1)$$

As can be seen from Figure 5b, the results show a pronounced dependence of the scratch parameters on the TiN/CrN ratio within the bilayer. The Λ30-TiN(20)/CrN(10) coating gave the highest values, L_{c1} = 14.4 N, L_{c2} = 17.7 N and CPR_s = 48 N^2. The Λ20-TiN(10)/CrN(10) coating has intermediate critical loads (L_{c1} = 10.9 N; L_{c2} = 14.4 N) and a relatively high CPR_s = 38 N^2 owing to the wider ΔL interval. The lowest crack propagation resistance was recorded for Λ30-TiN(10)/CrN(20) (L_{c1} = 11.6 N; L_{c2} = 14 N; CPR_s = 28 N^2), which is caused by the dominance of the more ductile and less stiff CrN phase [37,38]. The observed ranking correlates directly with the nanoindentation results (Figure 4): the maximum L_{c1} of Λ30-TiN(20)/CrN(10) corresponds to the maximum H = 25.1 GPa and H^3/E^2 = 0.186 GPa. The higher TiN volume fraction provides an increased load-bearing capacity of the coating in the zone of first cohesive failure owing to the stronger Ti-N covalent-ionic bonds compared with Cr-N [30]. The values CPR_s = 28–48 N^2 correspond to the typical range for thin (≈ 2.8 μm) nitride multilayers tested under progressive loading up to 30 N [30,39,40]. The much higher values CPR_s = 400–2000 N^2 reported for thick (10–15 μm) graded Cr/CrN/CrTiN architectures [41,42] are due mainly to the wider load range of the test (0–150 N) rather than to the toughness of the material itself. The ranking of the toughness characteristics is therefore as follows: Λ30-TiN(20)/CrN(10) > Λ20-TiN(10)/CrN(10) > Λ30-TiN(10)/CrN(20).

The optimum mechanical properties are reached not by minimizing the period within the studied Λ range, but by tuning the TiN/CrN layer thickness ratio while keeping the period close to, yet above, the superlattice peak region.

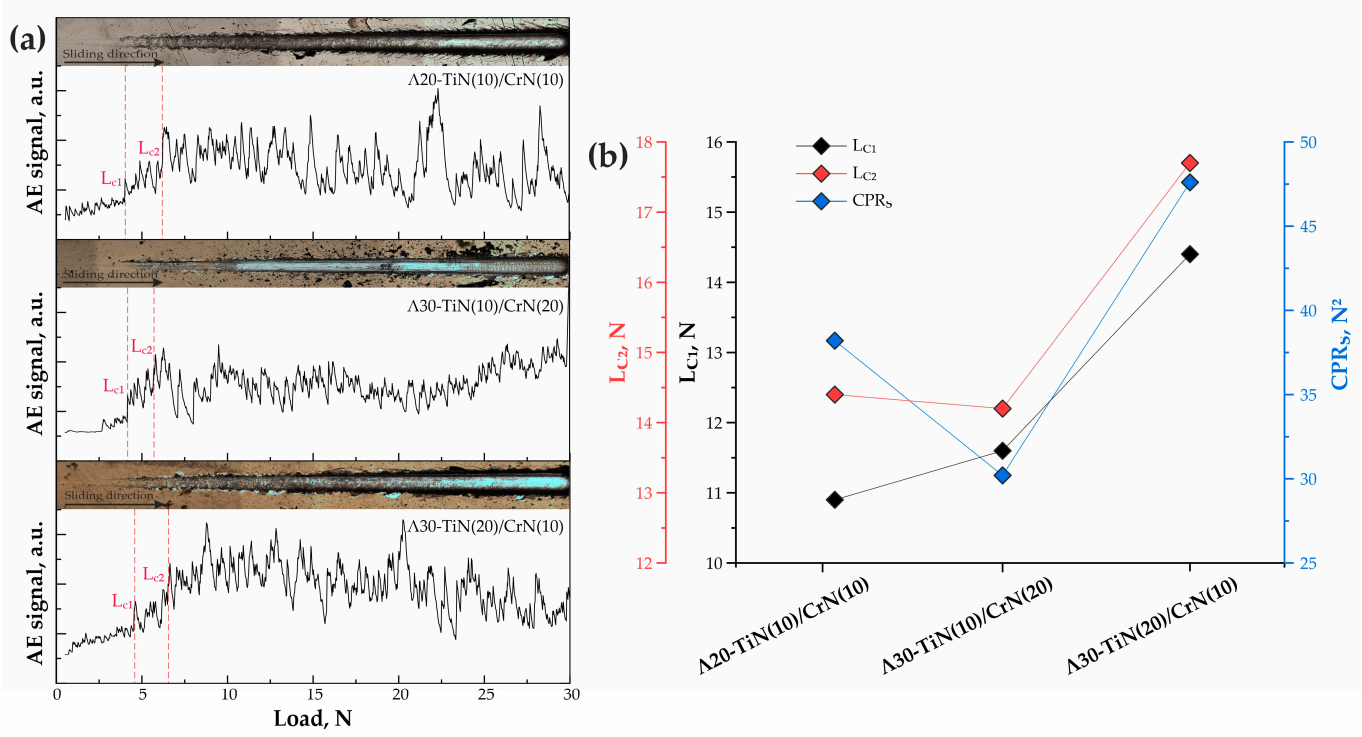

Figure 5. AE signals with optical images of the scratches (**a**) and a plot of the L_{C1}, L_{C2} and CPR_S data (**b**) for the TiN/CrN multilayers after the scratch test.

3.3. Analysis of the Tribological Characteristics of the TiN/CrN Multilayer Coatings

Figure 6a–b shows the COF and WR results of the TiN/CrN multilayers under dry friction and under lubricated friction. Each value was obtained by averaging three independent measurements. The results obtained show that a change in the bilayer architecture has a much stronger effect on the WR than on the COF.

Under dry sliding (Figure 6a), the lowest COF (0.59) belongs to Λ20-TiN(10)/CrN(10), whereas in terms of WR, the multilayer with the higher titanium nitride fraction, Λ30-TiN(20)/CrN(10), takes the lead. Increasing the CrN layer thickness to 20 nm at a TiN thickness of 10 nm (Λ30-TiN(10)/CrN(20)) sharply degrades the tribological characteristics: the WR rises by almost an order of magnitude and reaches 2.0×10^{-4} mm³/(N·m), while the COF simultaneously increases to 0.70. This is probably caused by the formation of more ductile Cr_2O_3 oxide films in the dry contact, which increase the adhesive component of friction. As a result, the WR increases, as noted in [24,25,37,43]. It should be noted that there is no direct correlation between COF and WR. Despite the higher COF of the Λ30-TiN(20)/CrN(10) coating, its WR is about 33% lower than that of the Λ20-TiN(10)/CrN(10) coating. The overall picture agrees well with the data in Section 3.2. The decisive factors are the map of the mechanical characteristics (Figure 4d) and the crack propagation resistance index (Figure 5b).

The transition to the boundary lubrication regime (Figure 6b) reduces the WR of all the coatings by about an order of magnitude, to $1.2–2.3\times10^{-5}$ mm³/(N·m), and the COF by a factor of 5–6, to the narrow range 0.114–0.116, even though the load was raised to 5 N. The practically identical COF of all three samples indicates that in the boundary regime, friction is governed mainly by the properties of the oil film rather than by the coating itself [44–46]. Under these conditions, the influence of the coating architecture on the COF almost disappears, whereas the differences in WR remain. The minimum WR of 1.2×10^{-5} mm³/(N·m) was again recorded for Λ30-TiN(20)/CrN(10), which reflects the mechanically controlled character of material loss even when the contacting surfaces are effectively sep-

arated by a lubricant film. The higher nanohardness and the maximum H^3/E^2 of this coating ensure minimum elastic-plastic deformation in the contact zone and, accordingly, the lowest WR [34,35].

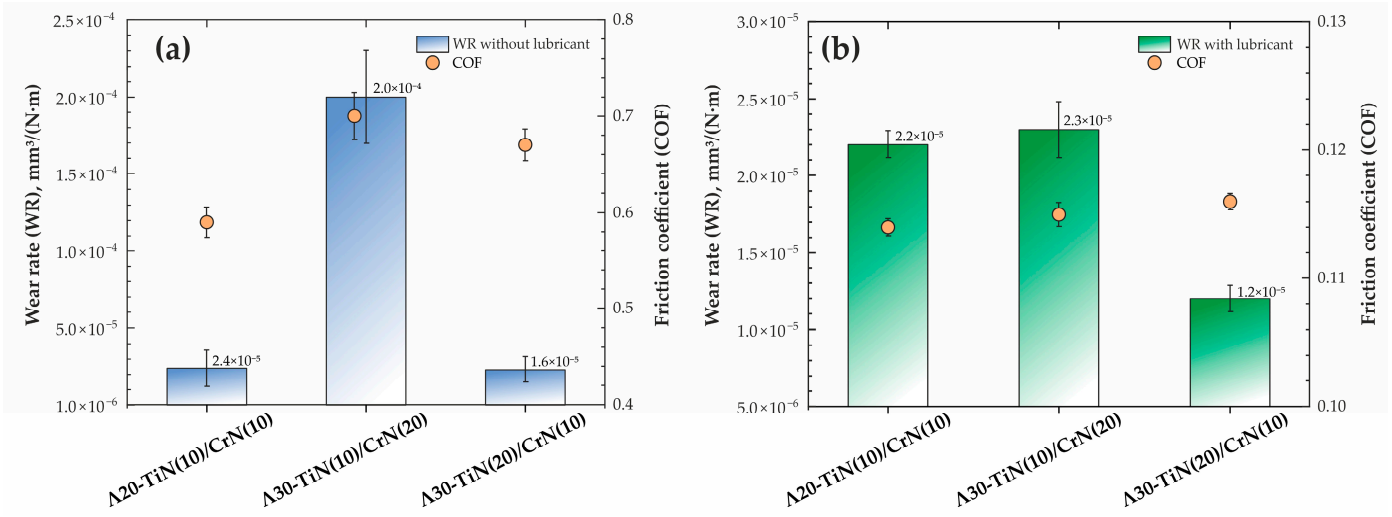

Figure 6. Tribological characteristics of the TiN/CrN multilayer coatings deposited on a 40Kh steel substrate: wear rate (WR, left axis, bars) and friction coefficient (COF, right axis, orange circles) obtained under (**a**) dry sliding and (**b**) boundary lubrication with the industrial oil TSP-15K.

Figure 7 presents three-dimensional optical profilometry of the wear tracks on the TiN/CrN multilayer coatings after tribological testing under dry sliding (left column) and under lubricated friction (right column). Each 3D image corresponds to one of the three selected scanning areas. Every panel shows the three-dimensional topography with a height colour scale in micrometres and the corresponding cross-sectional profile indicating the maximum track depth (h_{max}) and its width (W). The colour palettes of the height maps were chosen individually for each coating for the sake of visual discrimination. The cross-sectional profiles were taken along the lines marked with spherical markers on the 3D images. Optical micrographs of the same tracks are given as thumbnail insets.

Under dry conditions the wear depth increases in the order Λ30-TiN(20)/CrN(10) (h_{max} = 261 nm, W = 93 μm) < Λ20-TiN(10)/CrN(10) (324 nm, 82 μm) < Λ30-TiN(10)/CrN(20) (655 nm, 155 μm). This order reproduces the WR distribution (Figure 6a) and coincides with the ranking by mechanical and adhesion characteristics. The smallest track, obtained for Λ30-TiN(20)/CrN(10), corresponds to the maximum H (25.1 GPa), H^3/E^2 (0.186 GPa), L_{c1} (14.4 N), L_{c2} (17.7 N) and CPRs (48 N^2). The deepest track, obtained for Λ30-TiN(10)/CrN(20), corresponds to the minimum values of the same characteristics. According to the Leyland-Matthews and Musil criteria, high H/E and H^3/E^2 values limit the penetration depth of the counterbody, whereas a high CPRs restrains the propagation of cracks from the contact zone [34,35]. In the dry regime, the cross-sectional profile of Λ30-TiN(10)/CrN(20) has an uneven bottom with signs of spallation and local delamination, which reflects the transition to a catastrophic wear regime when the toughness of the coating is insufficient [38,39].

The transition to boundary lubrication changes the morphology of the tracks: the cross-sectional profiles become smooth and U-shaped, without signs of fracture. In the lubricated regime the track width (122–131 μm) exceeds that in the dry regime (82–93 μm) for the Λ20-TiN(10)/CrN(10) and Λ30-TiN(20)/CrN(10) samples, while h_{max} increases by a factor of 1.5–2.3. At first sight, this seems to contradict the order-of-magnitude decrease in WR (Figure 6b), but it is explained by the mechanics of the boundary regime: third-body particles retained by the oil exert a mild micro-polishing action that forms a wider

yet regular track, while the integral material loss decreases [44,46]. In addition, the load in the lubricated tests was 2.5 times higher.

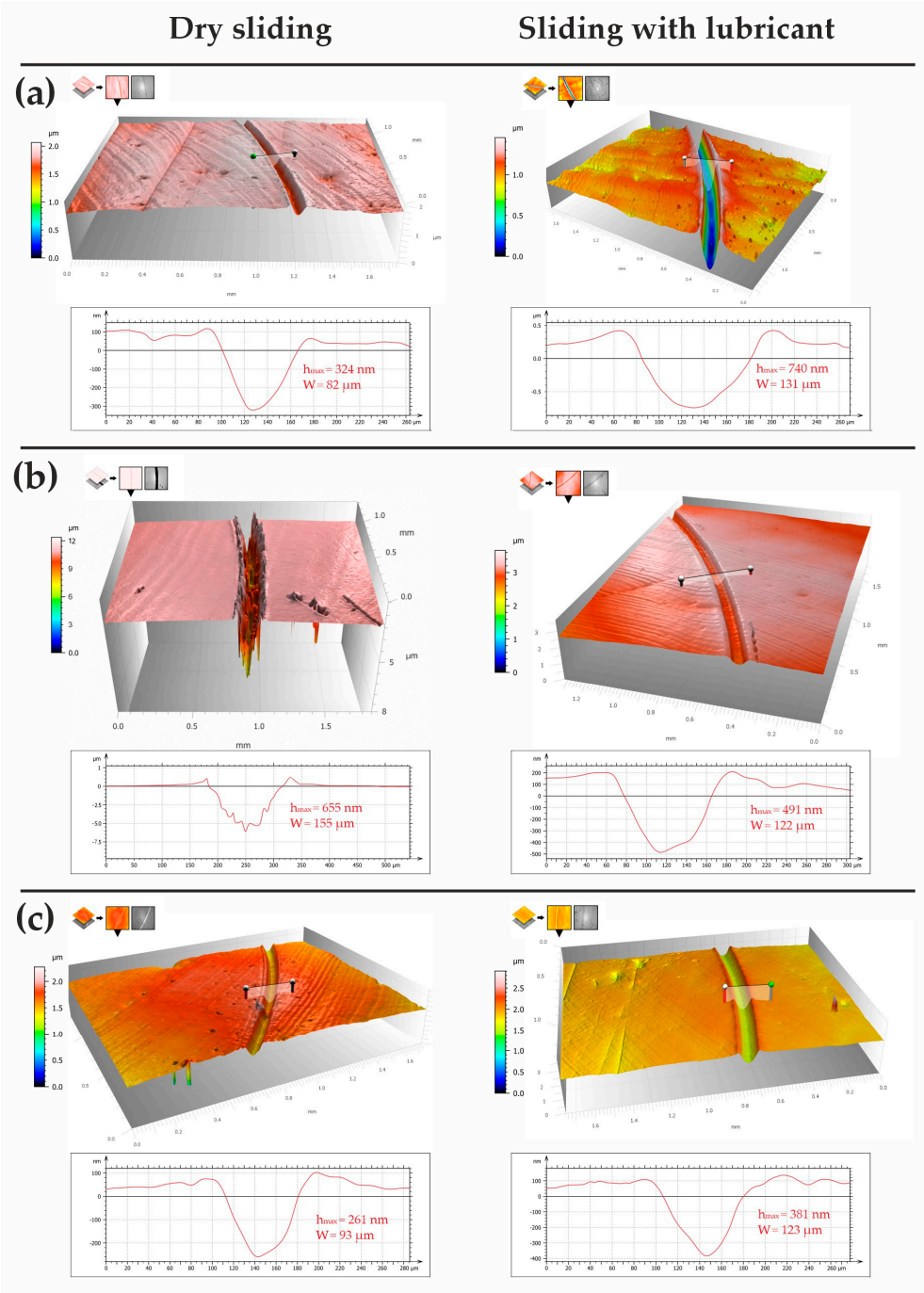

Figure 7. Three-dimensional optical profilometry of the wear tracks on the TiN/CrN multilayer coatings after testing under (left column) dry sliding and (right column) boundary lubrication with TSP-15K oil: (**a**) Λ20-TiN(10)/CrN(10); (**b**) Λ30-TiN(10)/CrN(20); (**c**) Λ30-TiN(20)/CrN(10).

3.4. Analysis of the Corrosion Characteristics of the TiN/CrN Multilayer Coatings

The corrosion resistance of a coating depends directly on its architecture. Figure 8 shows the potentiodynamic polarization curves (Tafel plots) recorded in 3.5 wt.% NaCl solution for the uncoated 40Kh steel substrate and for the three TiN/CrN multilayers. The curves reveal pronounced differences in the free corrosion potential (E_{corr}), in the extent of the quasi-passive region, and in the character of the anodic branch. The most noble $E_{corr} \approx -0.47$ V and the most extended quasi-passive region (up to ~3×10^{-5} A/cm^2) were recorded

for the Λ20-TiN(10)/CrN(10) coating; its anodic branch shows a gentle, extended rise in current density without abrupt breakdown. The uncoated steel shows an intermediate E_{corr} ≈ −0.51 V with a narrow quasi-passive region and an abrupt anodic breakaway at ~1.5×10⁻⁴ A/cm², typical of local breakdown of the passive oxide film on low-alloy steel in a chloride-containing medium [47]. The least noble E_{corr} ≈ −0.63 V and a monotonic rise in the anodic current from the lowest densities, without a pronounced plateau, are characteristic of Λ30-TiN(20)/CrN(10). For Λ30-TiN(10)/CrN(20) the curve shows a sharp rise in potential to ≈–0.28 V at a current density of ~5×10⁻⁴ A/cm², followed by a reversal towards more negative potentials as the current increases further. This is a characteristic hysteresis loop associated with the nucleation and avalanche-like growth of pitting [47]. The observed ranking of corrosion resistance is: Λ20-TiN(10)/CrN(10) > 40Kh steel > Λ30-TiN(20)/CrN(10) > Λ30-TiN(10)/CrN(20).

The TiN and CrN nitride layers are themselves electrochemically more noble than the steel, and the corrosion resistance of the system as a whole is determined not so much by their bulk inertness as by the density and connectivity of through-thickness growth defects (columnar boundaries, pores, microcracks) that give the electrolyte access to the substrate. Since the coating area (cathode) exceeds the defect area (anode) by orders of magnitude, a galvanic microcouple with a high cathode-to-anode area ratio forms at the defect, which localizes and accelerates the dissolution of the steel exactly at this point [46,48].

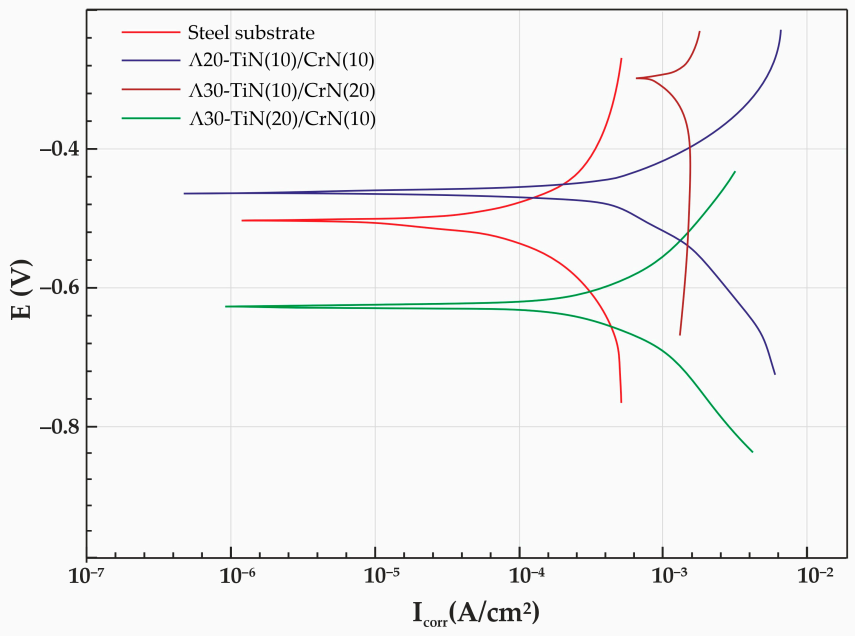

Figure 8. Potentiodynamic Tafel curves of the uncoated 40Kh steel and of the TiN/CrN multilayers in 3.5 wt.% NaCl solution.

The influence of the bilayer period agrees with the data of Section 3.1: at a similar total coating thickness (~2.8 μm), the period Λ20 corresponds to 130 bilayers (260 TiN/CrN interlayer boundaries), whereas Λ30 gives only 87 bilayers (173 boundaries). Each interface interrupts the columnar grain growth and deflects the growing defect sideways, reducing the probability of forming a through channel to the substrate. This is consistent with the most noble E_{corr} and the widest quasi-passive region recorded for Λ20-TiN(10)/CrN(10) [48–52].

Within the Λ30 group (Λ30-TiN(20)/CrN(10) and Λ30-TiN(10)/CrN(20)), the number of interlayer boundaries is the same, so the observed difference in corrosion behaviour is

governed by which sublayer dominates in thickness. For the Λ30-TiN(10)/CrN(20) coating, the most aggressive type of failure was recorded. This behaviour agrees with the results of Section 3.2, where precisely this architecture showed the lowest crack propagation resistance (CPR_S = 28 N^2, the lowest value in the series) because of the dominance of the more ductile and less stiff CrN phase [37,38]. Moreover, this sample had a low crystallinity, which increases the likelihood of a defective structure favourable to corrosion. For the Λ30-TiN(20)/CrN(10) coating, in contrast, a smooth anodic behaviour without pronounced breakdown is observed, which indicates a more distributed rather than concentrated character of the defects. The shift in E_{corr} towards more negative values (less noble than the steel itself) may reflect a mixed potential of the system that tends towards the potential of the steel because of the developed network of fine pores typical of the columnar TiN structure [26].

Thus, the architecture that is optimal in terms of corrosion resistance (small period, balanced TiN:CrN = 1:1 ratio) does not coincide with the architecture that is optimal in terms of the mechanical and tribological criteria (Λ30-TiN(20)/CrN(10), Sections 3.2–3.3). This agrees with the general logic of TiN/CrN multilayer design: TiN carries the main load and provides the load-bearing capacity, whereas CrN is responsible for ductility and corrosion resistance [8,17]; however, excessive thickening of the CrN sublayer in an architecture with sparse boundaries (Λ30) turns this contribution into its opposite: instead of increased resistance, localized catastrophic pitting occurs. The choice of the final coating architecture for practical application must therefore take into account the dominant type of loading: when the corrosion factor prevails, an architecture with a small period and balanced composition (Λ20-TiN(10)/CrN(10)) is preferable, whereas when mechanical or tribological loading prevails, an architecture with an increased TiN fraction (Λ30-TiN(20)/CrN(10)) is preferable.

4. Conclusions

Based on the comprehensive study of the structure, phase composition and mechanical, tribological and corrosion characteristics of TiN/CrN multilayer coatings deposited by pDCMS on 40Kh steel at bilayer periods of 20 and 30 nm and a varying thickness ratio of the constituent layers, the following conclusions can be drawn:

- A nitride structure based on TiN, CrN and the possible (Cr,Ti)N solid solution with predominant (200) growth orientation is formed in all the coatings; increasing the CrN fraction lowers the crystallinity of the coating (from 50% for Λ30-TiN(20)/CrN(10) to 28% for Λ30-TiN(10)/CrN(20)).
- Raising the TiN volume fraction increases the nanohardness, the elastic modulus and the plastic deformation resistance index H^3/E^2 (a maximum of 0.186 GPa, 52 times higher than that of the steel substrate), and also provides the best adhesion (L_{c1} = 14.4 N; L_{c2} = 17.7 N; CPR_S = 48 N^2) among the coatings studied.
- Under dry sliding, the lowest friction coefficient is shown by Λ20-TiN(10)/CrN(10) (0.59) and the lowest wear rate by Λ30-TiN(20)/CrN(10); thickening the CrN layer to 20 nm degrades the tribological characteristics by almost an order of magnitude because of the formation of ductile Cr_2O_3 oxide films. Under boundary lubrication, the differences in friction coefficient between the coatings practically disappear, whereas the differences in wear rate remain, which confirms the mechanically controlled character of the wear.
- The corrosion tests in 3.5 wt.% NaCl showed that the best protective ability (the most noble $E_{corr} \approx -0.47$ V, the most extended quasi-passive region) is provided by the coating with the smallest bilayer period and balanced composition, Λ20-TiN(10)/CrN(10), owing to the highest density of interlayer boundaries; thickening the CrN sublayer in an architecture with sparse boundaries (Λ30-TiN(10)/CrN(20))

provokes localized catastrophic pitting, whereas thickening the TiN sublayer (Λ30-TiN(20)/CrN(10)) leads to a more uniform active dissolution without abrupt breakdown.

Thus, the thickness ratio of the TiN and CrN layers at bilayer periods of 20 and 30 nm is an independent and effective tool for tuning the set of protective and antifriction properties of TiN/CrN multilayer coatings on structural steels.

Author Contributions: Conceptualization, K.S., A.K. and A.M. (Axaule Mamaeva); methodology, K.S., A.K. and D.K.; software, N.B.; validation, A.M. (Axaule Mamaeva) and P.K.; formal analysis, A.M. (Arailym Mukangaliyeva) and D.K.; investigation, K.S., A.K. and P.K.; resources, D.K.; data curation, A.K., N.B. and D.K.; writing—original draft preparation, A.K.; writing—review and editing, A.M. (Arailym Mukangaliyeva); visualization, A.M. (Axaule Mamaeva), P.K. and A.M. (Arailym Mukangaliyeva); supervision, A.K.; project administration, A.K.; funding acquisition, A.K. All authors have read and agreed to the published version of the manuscript.

Funding: This research is funded by the Science Committee of the Ministry of Science and Higher Education of the Republic of Kazakhstan (Grant № AP 26101617).

Institutional Review Board Statement: Not applicable.

Informed Consent Statement: Not applicable.

Data Availability Statement: The original contributions presented in this study are included in the article. Further inquiries can be directed to the corresponding authors.

Conflicts of Interest: The authors declare no conflicts of interest.

Abbreviations

The following abbreviations are used in this manuscript:

pDCMS	Pulsed DC magnetron sputtering
COF	Coefficient of friction
WR	Wear rate
SEM	Scanning electron microscopy
XRD	X-ray diffraction
H	Hardness
E	Elastic modulus
WDS	Wavelength-dispersive X-ray spectroscopy
CPRs	crack propagation resistance index

References

1. Xia, D.H.; Deng, C.M.; Macdonald, D.; Jamali, S.; Mills, D.; Luo, J.L.; Strebl, M.G.; Amiri, M.; Jin, W.; Song, S.; et al. Electrochemical measurements used for assessment of corrosion and protection of metallic materials in the field: A critical review. *J. Mater. Sci. Technol.* **2022**, *112*, 151–183. https://doi.org/10.1016/j.jmst.2021.11.004.
2. Mamayeva, A.A.; Kenzhegulov, A.K.; Panichkin, A.V.; Kshibekova, B.B.; Bakhytuly, N. Deposition of carbonitride titanium coatings by magnetron sputtering and its effect on tribo-mechanical properties. *Kompleks. Ispolz. Miner. Syra Complex Use Miner. Resour.* **2022**, *321*, 65–78. https://doi.org/10.31643/2022/6445.19.
3. Wang, Z.; Chen, X.; Gong, Y.; He, X.; Wei, Y.; Li, H. Tribocorrosion behaviours of cold-sprayed diamond–Cu composite coatings in artificial sea water. *Surf. Eng.* **2018**, *34*, 392–398. https://doi.org/10.1080/02670844.2017.1376821.
4. Holmberg, K.; Erdemir, A. Influence of tribology on global energy consumption, costs and emissions. *Friction* **2017**, *5*, 263–284. https://doi.org/10.1007/s40544-017-0183-5.
5. Jiang, G.; Cui, C.; Chen, L.; Wu, Y.; Cui, X. In situ synthesis of (M:Nb,Ta)C/Ni35 composite coating cladded on 40Cr steel. *Materials* **2021**, *14*, 7437. https://doi.org/10.3390/ma14237437.
6. Song, W.; Xia, Z.; Wang, S.; Zhang, X. Fabrication and tribological performance of Zr-coated carbide against 40Cr hardened steel. *Materials* **2018**, *11*, 1248. https://doi.org/10.3390/ma11071248.

7. Atmani, T.D.; Bouamerene, M.S.; Gaceb, M.; Nouveau, C.; Aknouche, H. Improvement of the tribological behavior of TiN/CrN multilayer coatings by modulation wavelength variation. *Tribol. Int.* **2024**, *192*, 109226. https://doi.org/10.1016/j.triboint.2023.109226.
8. Kenzhaliyev, B.; Kenzhegulov, A.; Mamaeva, A.; Panichkin, A.; Kshibekova, B.; Alibekov, Z.; Fischer, D. Tribological characteristics of multilayer TiN/TiCN coatings compared to TiN coatings. *J. Mater. Eng. Perform.* **2025**, *34*, 25810–25819. https://doi.org/10.1007/s11665-025-11182-w.
9. Totolin, V.; Pejaković, V.; Csanyi, T.; Hekele, O.; Huber, M.; Ripoll, M.R. Surface engineering of Ti6Al4V surfaces for enhanced tribocorrosion performance in artificial seawater. *Mater. Des.* **2016**, *104*, 10–18.
10. Bakhytuly, N.; Smailov, K.M.; Kenzhegulov, A.K.; Kudabayeva, M.A.; Yessengaziyev, A.M.; Karim, D.D.; Arynbayev, T.M. Deposition methods of multilayer hard coatings for improving tribological performance: A mini-review. Kompleks. *Ispolz. Miner. Syra Complex Use Miner. Resour.* **2027**, *343*, 16–33.
11. Hsu, C.H.; Lin, C.K.; Huang, K.H.; Ou, K.L. Improvement on hardness and corrosion resistance of ferritic stainless steel via PVD-(Ti,Cr)N coatings. *Surf. Coat. Technol.* **2013**, *231*, 380–384. https://doi.org/10.1016/j.surfcoat.2012.05.095.
12. Kenzhegulov, A.; Smailov, K.; Bakhytuly, N.; Karim, D.; Yessengaziyev, A.; Uskenbayeva, A.; Alibekov, Z. Effect of CrN layer composition on the microstructure, mechanical and tribological properties of TiN/CrN multilayer coatings. *Coatings* **2026**, *16*, 473.
13. Kenzhegulov, A.K.; Smailov, K.M.; Mamaeva, A.A.; Bakhytuly, N.; Uskenbayeva, A.M.; Alibekov, Z.Z. Investigation of the structure and composition of TiN and CrN coatings as a function of deposition parameters. *Kompleks. Ispolz. Miner. Syra Complex Use Miner. Resour.* **2028**, *344*, 55–64. https://doi.org/10.31643/2028/6445.06.
14. Atmani, T.D.; Gaceb, M.; Aknouche, H.; Nouveau, C.; Bouamrene, M.S. Parametric study of the mechanical properties of nanocrystalline TiN/CrN multilayer coatings with a special focus on the effect of coating thickness and substrate roughness. *Surf. Interfaces* **2021**, *23*, 101001. https://doi.org/10.1016/j.surfin.2021.101001.
15. Paulitsch, J.; Schenkel, M.; Schintlmeister, A.; Hutter, H.; Mayrhofer, P.H. Low friction CrN/TiN multilayer coatings prepared by a hybrid high power impulse magnetron sputtering/DC magnetron sputtering deposition technique. *Thin Solid Films* **2010**, *518*, 5553–5557. https://doi.org/10.1016/j.tsf.2010.05.061.
16. Tu, R.; Yuan, Y.; Yang, M.; Min, R.; Jiao, J.; Li, Q.; … Zhang, S. Effect of negative bias of HiPIMS and AIP hybrid deposition on microstructure, mechanical and anti-corrosive properties of Cr2N/TiN multilayer coatings. *Coatings* **2022**, *12*, 845.
17. Su, C.Y.; Pan, C.T.; Liou, T.P.; Chen, P.T.; Lin, C.K. Investigation of the microstructure and characterizations of TiN/CrN nano-multilayer deposited by unbalanced magnetron sputter process. *Surf. Coat. Technol.* **2008**, *203*, 657–660.
18. *GOST 4543-2016*; Metal Products from Structural Alloy Steel. Technical Conditions. 2017. Available online: https://files.stroyinf.ru/Data2/1/4293748/4293748469.pdf (accessed on 30 July 2026).
19. *GOST 19807-91*; Wrought Titanium and Titanium Alloys. Grades. 1991. Available online: http://vsegost.com/Catalog/28/28149.shtml (accessed on 30 July 2026).
20. *TU 14-22-164-2002*; Electrolytic Refined Chromium. Technical Conditions. 2002. Available online: https://nporusredmet.ru/product-category/redkozemelnye-i-redkie-metally/hrom/electro/ (accessed on 30 July 2026).
21. *ISO 14577*; Metallic Materials—Instrumented Indentation Test for Hardness and Materials Parameters. International Organization for Standardization: Geneva, Switzerland, 2015.
22. *DIN 50324*; Tribology; Testing of Friction and Wear Model Test for Sliding Friction of Solids (Ball on Disc System). German Institute for Standardisation: Berlin, Germany, 1992.
23. Stueber, M.; Holleck, H.; Leiste, H.; Seemann, K.; Ulrich, S.; Ziebert, C. Concepts for the design of advanced nanoscale PVD multilayer protective thin films. *J. Alloys Compd.* **2009**, *483*, 321–333.
24. Barshilia, H.C.; Jain, A.; Rajam, K.S. Structure, hardness and thermal stability of nanolayered TiN/CrN multilayer coatings. *Vacuum* **2004**, *72*, 241–248. https://doi.org/10.1016/j.vacuum.2003.08.003.
25. Paulitsch, J.; Maringer, C.; Mayrhofer, P.H. Low friction CrNMPP/TiNDCMS multilayer coatings. *Tribol. Lett.* **2012**, *46*, 87–93. https://doi.org/10.1007/s11249-012-9922-y.
26. Anders, A. A structure zone diagram including plasma-based deposition and ion etching. *Thin Solid Films* **2010**, *518*, 4087–4090.
27. Figueiredo, N.M.; Mateus, P.; Ponte, F.; Sharma, P.; Ferreira, J.; Cavaleiro, D.; Deuermeier, J.; Ferreira, F.; Cavaleiro, A.; Carvalho, S. Reducing the incorporation of contaminant oxygen in decorative TiN coatings deposited by low temperature reactive sputtering. *Vacuum* **2024**, *226*, 113325. https://doi.org/10.1016/j.vacuum.2024.113325.
28. Logothetidis, S.; Meletis, E.I.; Stergioudis, G.; Adjaottor, A.A. Room temperature oxidation behavior of TiN thin films. *Thin Solid Films* **1999**, *338*, 304–313. https://doi.org/10.1016/S0040-6090(98)00975-4.

29. Ou, Y.X.; Lin, J.; Tong, S.; Che, H.L.; Sproul, W.D.; Lei, M.K. Mechanical and tribological properties of CrN/TiN multilayer coatings deposited by pulsed dc magnetron sputtering. *Surf. Coat. Technol.* **2015**, *276*, 152–159. https://doi.org/10.1016/j.surfcoat.2015.06.064.
30. Zhang, S.; Li, J.; Tu, R.; Ando, K.; Gao, T. Improved hardness of semi-coherent TiN/CrN nano-multilayer coating through manipulation of structure evolution. *Mater. Sci. Eng. A* **2023**, *886*, 145728.
31. Pogrebnjak, A.D.; Bagdasaryan, A.A.; Yakushchenko, I.V.; Beresnev, V.M. The structure and properties of high-entropy alloys and nitride coatings based on them. *Russ. Chem. Rev.* **2014**, *83*, 1027–1061.
32. Cheng, Y.; Li, J.; Liu, F.; Li, H.; Yan, N. The mechanical performance enhancement of the CrN/TiAlCN coating on GCr15 bearing steel by controlling the nitrogen flow rate in the transition layer. *Coatings* **2025**, *15*, 254. https://doi.org/10.3390/coatings15030254.
33. Liu, Y.; Zhang, X.; Tu, M.; Hu, Y.; Wang, H.; Zhang, J.; Li, Z.; Zeng, X.; Wan, Q.; Vasiliy, P.; et al. Structure and mechanical properties of multi-principal-element (AlCrNbSiTi)N hard coating. *Surf. Coat. Technol.* **2022**, *433*, 128113. https://doi.org/10.1016/j.surfcoat.2022.128113.
34. Leyland, A.; Matthews, A. On the significance of the H/E ratio in wear control: A nanocomposite coating approach to optimised tribological behaviour. *Wear* **2000**, *246*, 1–11.
35. Musil, J. Hard nanocomposite coatings: Thermal stability, oxidation resistance and toughness. *Surf. Coat. Technol.* **2012**, *207*, 50–65.
36. Bharti, R.; Butt, M.; Dey, A. Nanoindentation and nanoscratch testing for the mechanical characterization of stealth thin film coatings. *Russ. J. Non-Ferr. Met.* **2024**, *65*, 151–161. https://doi.org/10.1134/S1067821224600686.
37. Leonov, A.A.; Denisova, Y.A.; Denisov, V.V.; Syrtanov, M.S.; Shmakov, A.N.; Savostikov, V.M.; Teresov, A.D. Structure and properties of CrN/TiN multi-layer coatings obtained by vacuum-arc plasma-assisted deposition method. *Coatings* **2023**, *13*, 351.
38. Azizpour, A.; Hahn, R.; Klimashin, F.F.; Wojcik, T.; Poursaeidi, E.; Mayrhofer, P.H. Deformation and cracking mechanism in CrN/TiN multilayer coatings. *Coatings* **2019**, *9*, 363.
39. Zhang, S.; Sun, D.; Fu, Y.; Du, H. Toughness measurement of thin films: A critical review. *Surf. Coat. Technol.* **2005**, *198*, 74–84.
40. Musil, J.; Kunc, F.; Zeman, H.; Poláková, H. Relationships between hardness, Young's modulus and elastic recovery in hard nanocomposite coatings. *Surf. Coat. Technol.* **2002**, *154*, 304–313.
41. Kabir, M.S.; Munroe, P.; Zhou, Z.; Xie, Z. Scratch adhesion and tribological behaviour of graded Cr/CrN/CrTiN coatings synthesized by closed-field unbalanced magnetron sputtering. *Wear* **2017**, *380–381*, 163–175. https://doi.org/10.1016/j.wear.2017.03.020.
42. Lan, Z.; Deng, J.; Xu, H.; Xu, Z.; Wen, Z.; Long, W.; Zhang, L.; Wang, R.; Liu, J.; Chen, Y. The oxidation and corrosion resistance of AlCrNbSiTiN multi-principal element nitride coatings. *Materials* **2025**, *18*, 4663.
43. Holmberg, K.; Matthews, A. *Coatings Tribology: Properties, Mechanisms, Techniques and Applications in Surface Engineering*; Elsevier: Amsterdam, The Netherlands, 2009; Volume 56.
44. Podgornik, B.; Sedlaček, M.; Mandrino, D. Performance of CrN coatings under boundary lubrication. *Tribol. Int.* **2016**, *96*, 247–257. https://doi.org/10.1016/j.triboint.2015.12.039.
45. Bakhytuly, N.; Kenzhegulov, A.; Nurtanto, M.; Aliev, A.; Kuldeev, E. Microstructure and tribological study of TiAlCN and TiTaCN coatings. *Kompleks. Ispolz. Miner. Syra = Complex Use Miner. Resour.* **2023**, *327*, 99–110.
46. Erdemir, A. Review of engineered tribological interfaces for improved boundary lubrication. *Tribol. Int.* **2005**, *38*, 249–256. https://doi.org/10.1016/j.triboint.2004.08.008.
47. Marulanda, D.M.; Olaya, J.J.; Piratoba, U.; Mariño, A.; Camps, E. The effect of bilayer period and degree of unbalancing on magnetron sputtered Cr/CrN nano-multilayer wear and corrosion. *Thin Solid Films* **2011**, *519*, 1886–1893.
48. Liu, C.; Leyland, A.; Bi, Q.; Matthews, A. Corrosion resistance of multi-layered plasma-assisted physical vapour deposition TiN and CrN coatings. *Surf. Coat. Technol.* **2001**, *141*, 164–173.
49. Ahn, S.H.; Lee, J.H.; Kim, J.G.; Han, J.G. Localized corrosion mechanisms of the multilayered coatings related to growth defects. *Surf. Coat. Technol.* **2004**, *177–178*, 638–644.
50. Yessengaziyev, A.; Mukangaliyeva, A.; Toishybek, A.; Karshyga, Z.; Abdyldayev, N.; Yersaiynova, A.; Bakhytuly, N. Studies the crucial role of selection of extractant to extract niobium from sulfuryl fluoride solution and optimization of extraction conditions. *Acta Metall. Slovaca* **2024**, *30*, 120–126. https://doi.org/10.36547/ams.30.3.2060.
51. Yessengaziyev, A.; Toishybek, A.; Mukangaliyeva, A.; Abdyldayev, N.; Yersaiynova, A. Study of the leaching process for dust chamber sublimates followed by the extraction of niobium and zirconium into solution. *Kompleks. Ispolz. Miner. Syra = Complex Use Miner. Resour.* **2024**, *331*, 117–126. https://doi.org/10.31643/2024/6445.45.

52. Chipatecua, Y.L.; Olaya, J.J.; Arias, D.F. Corrosion behaviour of CrN/Cr multilayers on stainless steel deposited by unbalanced magnetron sputtering. *Vacuum* **2012**, *86*, 1393–1401.